AGU PUBLICATIONS

JGR

Journal of Geophysical Research: Solid Earth

RESEARCH ARTICLE
10.1002/2016JB013136

Key Points:
- Elastic constants of Fe-free and Fe-bearing NAL phase at high pressures have been determined
- NAL phase exhibits high-velocity anisotropies at pressures of the uppermost lower mantle
- NAL phase may contribute to the observed seismic anisotropy in the uppermost lower mantle

Supporting Information:
- Supporting Information S1

Correspondence to:
X. Wu, and J.-F. Lin,
wuxiang@cug.edu.cn;
afu@jsg.utexas.edu

Citation:
Wu, Y., J. Yang, X. Wu, M. Song, T. Yoshino, S. Zhai, S. Qin, H. Huang, and J.-F. Lin (2016), Elasticity of single-crystal NAL phase at high pressure: A potential source of the seismic anisotropy in the lower mantle, *J. Geophys. Res. Solid Earth*, *121*, doi:10.1002/2016JB013136.

Received 30 APR 2016
Accepted 29 JUL 2016
Accepted article online 1 AUG 2016

Elasticity of single-crystal NAL phase at high pressure: A potential source of the seismic anisotropy in the lower mantle

Ye Wu[1,2], Jing Yang[3], Xiang Wu[2,4], Maoshuang Song[5], Takashi Yoshino[6], Shuangmeng Zhai[7], Shan Qin[2], Haijun Huang[1], and Jung-Fu Lin[3,8]

[1]School of Science, Wuhan University of Technology, Wuhan, China, [2]Key Laboratory of Orogenic Belts and Crustal Evolution, MOE, School of Earth and Space Sciences, Peking University, Beijing, China, [3]Department of Geological Sciences, Jackson School of Geosciences, University of Texas at Austin, Austin, Texas, USA, [4]State Key Laboratory of Geological Processes and Mineral Resources, China University of Geosciences, Wuhan, China, [5]State Key Laboratory of Isotope Geochemistry, Guangzhou Institute of Geochemistry, Chinese Academy of Sciences, Guangzhou, China, [6]Institute for Study of the Earth's Interior, Okayama University, Misasa, Japan, [7]Key Laboratory of High-Temperature and High-Pressure Study of the Earth's Interior, Institute of Geochemistry, Chinese Academy of Sciences, Guiyang, China, [8]Center for High Pressure Science and Technology Advanced Research (HPSTAR), Shanghai, China

Abstract The new hexagonal aluminous phase, named the NAL phase, is expected to be stable at depths of <1200 km in subducted slabs and believed to constitute 10~30 wt% of subducted mid-ocean ridge basalt together with the $CaFe_2O_4$-type aluminous phase. Here elasticity of the single-crystal NAL phase is investigated using Brillouin light scattering coupled with diamond anvil cells up to 20 GPa at room temperature. Analysis of the results shows that the substitution of iron lowers the shear modulus of the NAL phase by ~5% (~6 GPa) but does not significantly affect the adiabatic bulk modulus. The NAL phase exhibits high-velocity anisotropies with $AV_P = 14.7\%$ and $AV_S = 15.12\%$ for the Fe-bearing phase at ambient conditions. The high AV_S of the NAL phase mainly results from the high anisotropy of the faster V_{S1} (13.9~15.8%), while the slower V_{S2} appears almost isotropic (0.1~2.8%) at ambient and high pressures. The AV_P and AV_S of the NAL phase decrease with increasing pressure but still have large values with $AV_P = 11.4\%$ and $AV_S = 14.12\%$ for the Fe-bearing sample at 20.4 GPa. The extrapolated AV_P and AV_S of the Fe-free and Fe-bearing NAL phases at 40 GPa are larger than those of bridgmanite at the same pressure. Together with its spin transition of iron and structural transition to the CF phase, the presence of the NAL phase with high-velocity anisotropies may contribute to the observed seismic anisotropy around subducted slabs in the uppermost lower mantle.

1. Introduction

The fate of subducted slabs in the Earth's mantle has been a central issue relevant to our understanding of the geodynamic processes and chemical evolution of the Earth. Tomographic images around the circum-Pacific regions have revealed that subducted slabs can penetrate into the deep mantle and not only stagnate near the 660 km discontinuity, but also accumulate at the bottom of the lower mantle [*Fukao and Obayashi*, 2013; *Zhao*, 2004]. High-pressure and high-temperature studies on the subducted mid-ocean ridge basalt (MORB) have shown that it is denser than the surrounding peridotite, which can provide sufficient density contrast to drive the slabs into the lowermost mantle [*Hirose et al*., 2005; *Ono et al*., 2005; *Ricolleau et al*., 2010]. It has also been suggested that seismic signatures observed in the lower mantle, including seismic anisotropies, discontinuities, and scatterers, could be related to the presence of subducted slabs [*Kaneshima*, 2013; *Kawakatsu and Niu*, 1994; *Wookey et al*., 2002]. To better understand the geodynamics of the mantle and the fate of subducted slabs, it is thus essential to study the physical and chemical properties of the candidate minerals in subducted slabs at relevant pressure-temperature conditions of the lower mantle.

As compared to mantle peridotite, MORB is enriched in aluminum, silicon, calcium, and sodium elements but depleted in magnesium [*Green et al*., 1979; *Sun*, 1982]. Its high Al_2O_3 content of ~16 wt% stabilizes the aluminous phases, calcium-ferrite (CF)-type phase (space group: *Pbnm*) and new hexagonal aluminous (NAL) phase (space group: $P6_3/m$) [*Irifune and Ringwood*, 1993; *Miyajima et al*., 1999]. The NAL and CF phases coexist at 25~50 GPa and constitute 10~30 wt% of the subducted MORB [*Hirose and Fei*, 2002; *Ricolleau et al*., 2010].

Studies on the inclusions in diamonds from Juina-5 kimberlite directly verify the presence of the NAL and CF phases in subducted slabs in the lower mantle [*Walter et al*., 2011].

The high amount of the aluminous phases in the MORB has attracted considerable attention from researchers to investigate their phase stabilities, physical and chemical properties, as these properties are important to our understanding of the geophysics and geochemistry of the subducted basaltic slabs in the lower mantle [*Guignot and Andrault*, 2004; *Imada et al*., 2011; *Kawai and Tsuchiya*, 2012; *Ono et al*., 2009; *Ricolleau et al*., 2010; *Wu et al*., 2016]. Studies on the phase relations of natural MORB indicate that both the NAL and CF phases coexist up to ~50 GPa, but only the CF phase is observed beyond 50 GPa [*Ricolleau et al*., 2010]. The CF phase is identified as a high-pressure phase of the NAL phase in the $NaAlSiO_4$-$MgAl_2O_4$ system [*Imada et al*., 2011; *Ono et al*., 2009]. Experimental studies on sound velocities of polycrystalline NAL and CF samples using Brillouin light scattering (BLS) show that shear wave velocity increases by 2.5% upon the NAL to CF phase transition at ~40 GPa [*Dai et al*., 2013]. First-principle calculations on the elastic properties of the NAL and CF phases indicate that the shear wave anisotropy increases dramatically from 13.3% to 22.1% across the transition, which could be seismically detectable [*Kawai and Tsuchiya*, 2012]. In addition, single-crystal BLS measurements on the NAL phase at ambient conditions show that it displays elastic compression and shear waves anisotropies of 13.9%, which are relatively high compared to other lower mantle minerals [*Pamato et al*., 2014]. However, experimental results on single-crystal elastic and seismic properties of the NAL and CF phases at lower mantle conditions are required to understand the seismic profiles of the subducted slabs in the lower mantle.

In this study, we investigated the single-crystal elasticity of the two NAL phase samples, Fe bearing and Fe free, at pressures up to 20 GPa and room temperature using BLS coupled with diamond anvil cells (DACs). We show results of the elastic and velocity properties of the Fe-free and Fe-bearing NAL phases and discuss the effects of iron on the velocity anisotropies and heterogeneity ratios of the NAL phase in the lower mantle. These results are used to discuss potential geophysical implications for the seismic anisotropy of subducted slabs with the presence of the NAL phase in the lower mantle.

2. Experimental Methods

High-quality single crystals of the Fe-free and Fe-bearing NAL phases were synthesized at high P-T conditions using a multianvil apparatus (run nos. 5K2283 and 5K2420) [*Wu et al*., 2016]. Lattice parameters of the Fe-free sample ($Na_{1.14}Mg_{1.83}Al_{4.74}Si_{1.23}O_{12}$) at ambient conditions are $a = b = 8.736(5)$ Å, $c = 2.770(1)$ Å, and $V = 183.1(1)$ Å^3, while the Fe-bearing sample ($Na_{0.71}Mg_{2.05}Al_{4.62}Si_{1.16}Fe^{2+}_{0.09}Fe^{3+}_{0.17}O_{12}$) has $a = b = 8.762(4)$ Å, $c = 2.7789(8)$ Å, and $V = 184.76(6)$ Å^3.

High-pressure BLS experiments at room temperature were performed on both Fe-free and Fe-bearing NAL samples at the Mineral Physics Laboratory of the University of Texas at Austin. The Brillouin system was equipped with a Coherent Verdi V2 laser with a wavelength of 532 nm, a JRS six-pass tandem Fabry-Perot interferometer, and a COUNT-10B avalanche photodiode detector with a low dark count rate of $\leq$5 c/s at room temperature. The laser beam was focused to approximately 20 μm in diameter on the sample in a DAC. The Brillouin scattering angle was set up to 46.8°, which was calibrated using a number of standard calibrants including silica glass, distilled water, and single-crystal MgO [*Lu et al*., 2013; *Yang et al*., 2015]. Two short symmetric diamond anvil cells equipped with 400 μm diameter diamond culets were used for the high-pressure BLS measurements. A rhenium gasket was preindented to 40~50 μm in thickness. Subsequently, a hole of approximately 270 μm in diameter was drilled in the preindented gasket and used as the sample chamber. The NAL single crystals exhibit hexagonal prism shape, which permitted us to use a stereo microscope to identify their *x*-*z* and *x*-*y* crystallographic planes. The orientation of these preidentified platelets at ambient conditions were further examined and confirmed using single-crystal X-ray diffraction (XRD) before they were loaded into DACs for high-pressure Brillouin experiments. For Fe-bearing NAL phase, *x*-*z* plane is determined to be (−0.05, 0, 1) and *x*-*y* plane is (0.03, 1, 0). For Fe-free NAL phase, *x*-*z* plane is (0.04, −0.02, 1) and *x*-*y* plane is (1, −0.07, −0.09). Two single-crystal platelets of 60~80 μm in diameter and 20 μm in thickness for each composition were loaded into the sample chamber, together with neon gas pressure transmitting medium and several ruby spheres for pressure calibration (Figure 1a inserted figure) [*Mao et al*., 1986]. Pressures were measured from the ruby fluorescence spectra, while pressure uncertainties were determined from the pressures before and after the BLS measurements for each pressure point. For each platelet (*x*-*z* or *x*-*y* plane) at each given pressure, Brillouin spectra were collected in 19

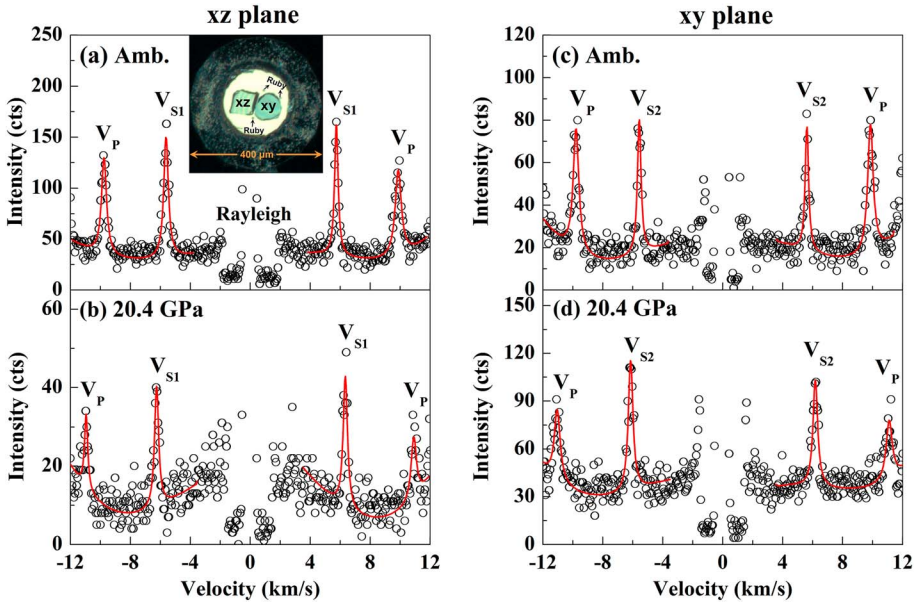

Figure 1. Representative Brillouin spectra of the (a and b) *x-z* and (c and d) *x-y* planes for the single-crystal Fe-bearing NAL phase at ambient conditions and 20.4 GPa. The inserted figure in Figure 1a is a representative photo of the two crystal platelets in the sample chamber at ~3 GPa and 300 K.

different crystallographic directions from 0 to 180° of the azimuthal angle at an interval of 10°. The BLS experiments on the NAL phase were performed up to 20 GPa at room temperature at a pressure interval of 2~3 GPa.

3. Results and Discussion

3.1. Elastic Properties of the NAL Phase

The measured BLS spectra showed strong *P* wave (V_P) and *S* waves (V_{S1} and V_{S2}) with a high signal-to-noise ratio (Figures 1 and S1 in the supporting information). Although the *P* wave and two polarized *S* waves were expected to exist in the anisotropic single crystal, only the V_P and the faster polarizing V_{S1} were observed for the *x-z* plane, while the V_P and lower V_{S2} were detected from the *x-y* plane. These are likely a result of the polarization of the shear waves in the hexagonal crystal interacting with the incident laser. The measured V_P and V_{S1} of the *x-z* plane varied significantly by a maximum amplitude of 1.3~1.6 km/s as a function of the azimuthal angle, but no notable variation in of the V_P and V_{S2} were observed for the *x-y* plane. These observations indicate a high elastic anisotropy within the *x-z* plane and almost isotropic behavior for the *x-y* plane in the NAL phase (Figures S2 and S3). Furthermore, both V_P and V_S of the NAL phase increase with increasing pressure, and the V_P at some crystallographic directions overlap with the V_S of the diamond anvils starting at ~10 GPa. With the current experimental Brillouin capabilities we have access to, it is difficult to determine elastic constants of the NAL phase at pressures above 20 GPa.

Single-crystal elastic constants (C_{ij}) of the NAL phase at each given pressure were evaluated by the best fit of the measured acoustic velocities at various crystallographic directions along the *x-z* and *x-y* planes using the Christoffel's equation (Figure 2 and Table S1 in the supporting information) [*Every*, 1980]:

$$\left|C_{ijkl}n_jn_l - \rho V^2\delta_{ik}\right| = 0, \quad (1)$$

where C_{ijkl} are the elastic constants in full suffix notation, n_i represents the direction cosine of the phonon propagation direction and are described by three Eulerian angles (θ, χ, and ϕ), V is the measured acoustic velocity, δ_{ik} is the Kronecker delta [*Musgrave*, 1970], and ρ is the density from our previous single-crystal XRD measurements [*Wu et al.*, 2016]. The calculated acoustic velocities from the best fit elastic model are in excellent agreement with the experimental velocities at ambient conditions and high pressures (Figures S2 and S3). Five independent elastic constants (C_{11}, C_{12}, C_{13}, C_{33}, and C_{44}) of the NAL phase increase smoothly with increasing pressure (Figure 2 and Table S1). The NAL phase exhibits extremely large

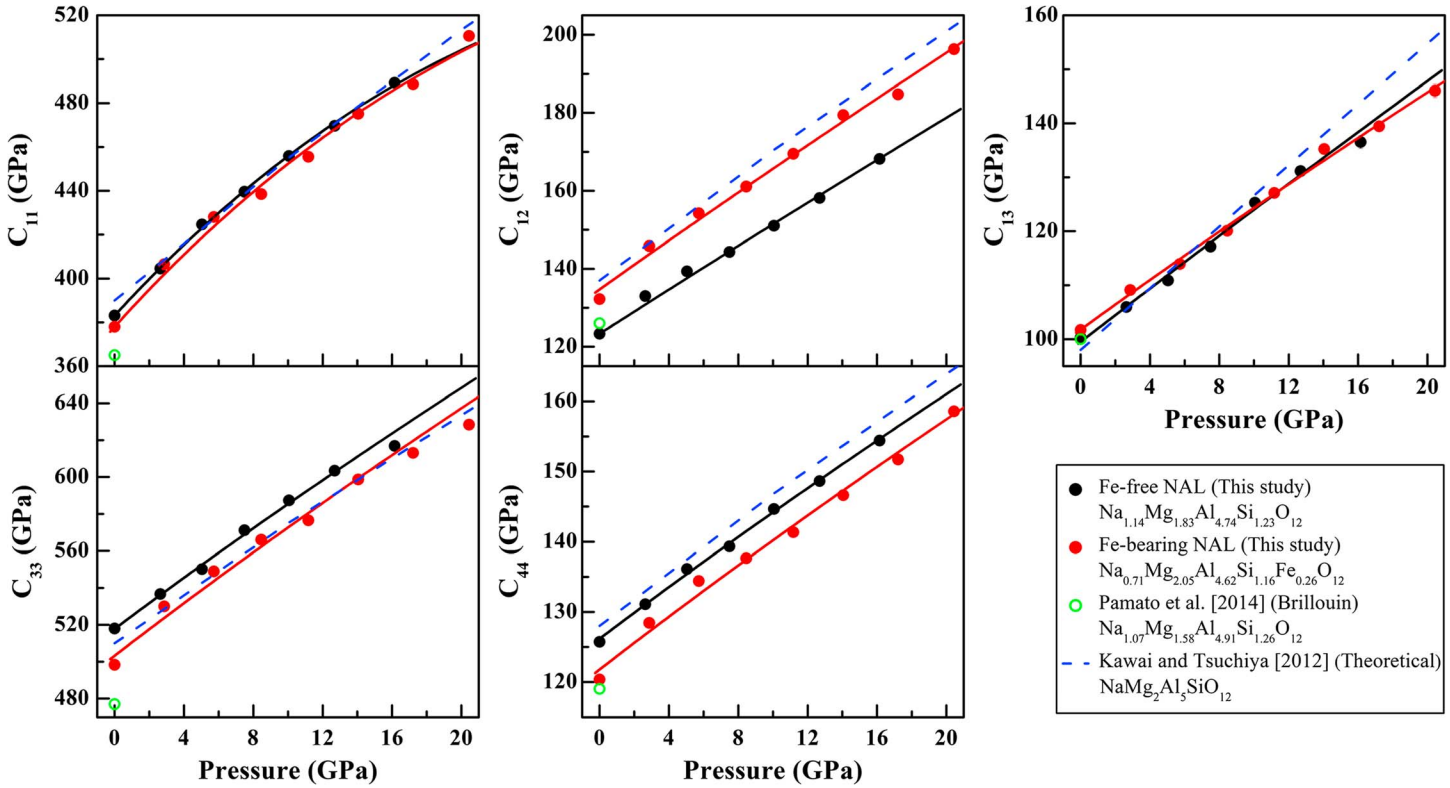

Figure 2. Single-crystal elastic constants of the NAL phase at high pressures and room temperature. Black circles and lines: experimental data and modeled results of the Fe-free NAL phase, respectively (this study); red circles and lines: Fe-bearing NAL phase (this study); green open circles: *Pamato et al.* [2014]; blue dash lines: *Kawai and Tsuchiya* [2012].

longitudinal elastic constants C_{11} and C_{33} at ambient conditions, $C_{11} = 383.1(3)$ GPa and $C_{33} = 518.0(7)$ GPa for Fe-free NAL sample and $C_{11} = 378.0(3)$ GPa and $C_{33} = 498.3(6)$ GPa for Fe-bearing NAL. These results reveal a large anisotropy in the axial incompressibility along *a* axis and *c* axis compared with other elastic constants. The *a* axis is more compressible than *c* axis with $C_{11} < C_{33}$ for the NAL phase. These results are consistent with recent results on the axial incompressibility of the NAL phase derived from high-pressure, single-crystal XRD measurements on the same materials [*Wu et al.*, 2016]. The large anisotropy in the axial incompressibility of the NAL phase can be related to the arrangement of octahedrons in the crystal structure. The crystal structure consists of octahedral chains by edge sharing along the *c* axis direction, while adjacent chains share edges and corners perpendicular to the *c* axis to form two kinds of tunnels with hexagonal and ditrigonal cross sections, respectively [*Miura et al.*, 2000]. The arrangement of the octahedral chain framework makes the *c* axis direction more resistant to compression than the *a* axis direction. The substitution of iron in the NAL phase causes a decrease of the diagonal elastic constants, C_{11}, C_{33}, and C_{44} by 1.3%, 4.0%, and 4.5%, respectively, and an increase in the off-diagonal C_{12} by 6.7%, but does not affect C_{13} significantly. Compared to Fe-free NAL phase, 22% Fe^{2+} and 50% Fe^{3+} of the total iron ions substitute for Mg^{2+} in the trigonal prismatic site of the Fe-bearing NAL phase, while the remaining 28% Fe^{3+} and Mg^{2+} ions substitute for Al^{3+} and Si^{4+} in the octahedral site [*Wu et al.*, 2016]. Since the ionic radii of the major cations are $R(Fe^{2+}\text{-HS}) > R(Mg^{2+}) > R(Fe^{3+}\text{-HS})$ and $R(Fe^{3+}\text{-HS}) > R(Al^{3+}) > R(Si^{4+})$ [*Shannon*, 1976], the unit-cell volume of the Fe-bearing NAL phase is larger than that of Fe-free NAL phase. The elastic constants C_{11} and C_{33} are the compression components of *a* and *c* axes, respectively, and C_{44} is the shear component of *a* axis. Thus, the *a* and *c* axes of the Fe-bearing NAL phase are more compressible than that of the Fe-free NAL phase. In other words, the substitution of iron in the NAL phase causes a decrease in the diagonal elastic constants (C_{11}, C_{33}, and C_{44}).

Using the derived elastic constants of the NAL phase, the adiabatic bulk and shear moduli (K_S and G) at ambient conditions and high pressures were calculated according to the Voigt-Reuss-Hill averages (Figure 3 and Table S1) [*Hill*, 1952]. The derived K_S and G at ambient conditions are $K_{S0} = 213.5(4)$ GPa and $G_0 = 138.4(2)$ GPa

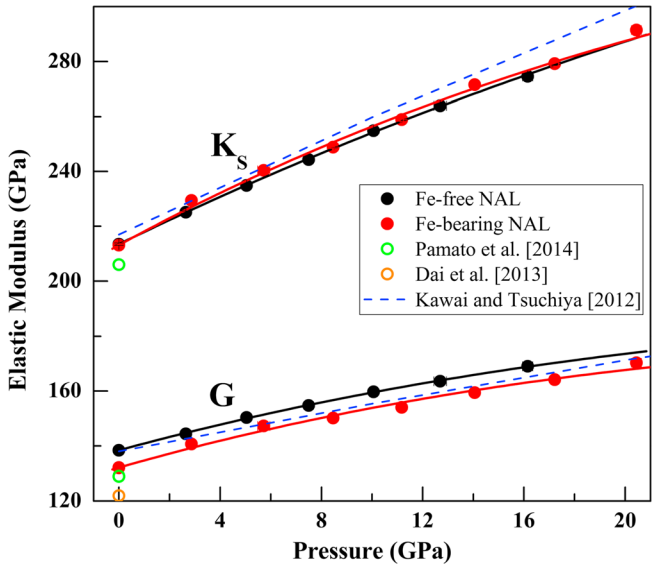

Figure 3. Adiabatic bulk and shear moduli (K_S and G) of the NAL phase at high pressures and room temperature. Black circles and lines: experimental data and modeled results of the Fe-free NAL phase, respectively (this study); red circles and lines: Fe-bearing NAL phase (this study); open circles: *Pamato et al.* [2014] and *Dai et al.* [2013]; blue dash lines: *Kawai and Tsuchiya* [2012].

for the Fe-free NAL phase and $K_{S0} = 213.1(3)$ GPa and $G_0 = 132.1(1)$ GPa for the Fe-bearing NAL. The substitution of iron in the NAL phase does not significantly affect the K_S, but slightly reduces G by ~5% (~6 GPa). An iterative procedure was adopted to determine the pressure derivatives of the elastic moduli as well as the density at each pressure point for the NAL phase. An initial density model from our previous XRD measurement on the NAL phase was used to obtain K_{S0} and its first-order pressure derivative $(\partial Ks/\partial P)_T$ from a least squares fit to the Eulerian finite strain equation [*Birch*, 1978]. The derived K_{S0} and $(\partial Ks/\partial P)_T$ were then used to calculate the corresponding isothermal bulk modulus K_{T0} and its first-order pressure derivative $(\partial K_T/\partial P)_T$ using the following thermodynamic relations [*Poirier*, 2000]:

$$K_{T0} = K_{S0}/\ (1\ + \alpha\gamma T); \tag{2}$$

$$(\partial K_T/\partial P)_T = \ (1\ + \alpha\gamma T)^{-1}\left[(\partial Ks/\partial P)_T - (\gamma T/K_{T0})\ (\partial K_T/\partial T)_P\right], \tag{3}$$

where α is the thermal expansion coefficient, γ is the Grüneisen parameter, and $(\partial K_T/\partial T)_P$ is the temperature derivative of K_T at constant pressure. Thermodynamic parameters from literature were used for aforementioned calculations: $(\partial K_T/\partial T)_P = -0.020(2)$ GPa/K and $\alpha = 3.28(7)\times10^{-5} + 3.0(9)\times10^{-9}T$ [*Shinmei et al.*, 2005]; $\gamma = \alpha K_T V_T/(\alpha^2 K_T V_T T - C_P)$ with C_P (300 K) = 120.7 J/mol/K [*Ono et al.*, 2009]. The derived K_{T0} and $(\partial K_T/\partial P)_T$ were then used to construct the isothermal compression curve and to obtain refined densities. The iterative procedure was repeated until the refined densities were self-consistent with the initial densities.

Third-order Eulerian finite strain equations were used to obtain the first-order pressure derivatives of C_{12}, C_{13}, C_{33}, and C_{44} (Figure 2), yielding $(\partial C_{12}/\partial P)_T = 2.71(7)$, $(\partial C_{13}/\partial P)_T = 2.44(8)$, $(\partial C_{33}/\partial P)_T = 6.9(2)$, and $(\partial C_{44}/\partial P)_T = 1.84(4)$ for the Fe-free NAL phase and $(\partial C_{12}/\partial P)_T = 3.1(1)$, $(\partial C_{13}/\partial P)_T = 2.29(5)$, $(\partial C_{33}/\partial P)_T = 7.1(4)$, and $(\partial C_{44}/\partial P)_T = 1.88(8)$ for the Fe-bearing NAL phase (Table S2). Since the longitudinal elastic modulus C_{11}, K_S, and G clearly exhibit a pressure-dependent derivative, they were fitted to the fourth-order finite strain equations (Figures 2 and 3), yielding the first and second pressure derivatives of elastic moduli listed in Table S2. Analysis of these results show that the substitution of iron does not produce a distinct effect on the $(\partial M/\partial P)_T$ and $(\partial M/\partial P)_T^2$ ($M = C_{ij}$, K_S, or G).

3.2. Velocity Properties of the NAL Phase

The derived elastic constants of the NAL phase can be used to evaluate a number of key seismic parameters at high pressures. The azimuthal velocity anisotropy describes the velocity as a function of the wave propagation direction (Figure 4). The derived velocity propagation, normal and parallel to the c axis (x-y and x-z planes, respectively), shows that the V_P propagates fastest along the [0001] direction and slowest along directions perpendicular to the c axis. Additionally, V_{S1} is fastest along the diagonal directions of the [0 $\bar{1}$ 10] and [0001], while V_{S2} has almost identical values in different directions. These results indicate that the NAL phase exhibits high anisotropies of V_P and V_{S1}, whereas V_{S2} is almost isotropic.

To understand the evolution of velocity anisotropy of the NAL phase as a function of pressure, velocities for different propagation directions and anisotropy distributions are calculated from the C_{ij} and density at each

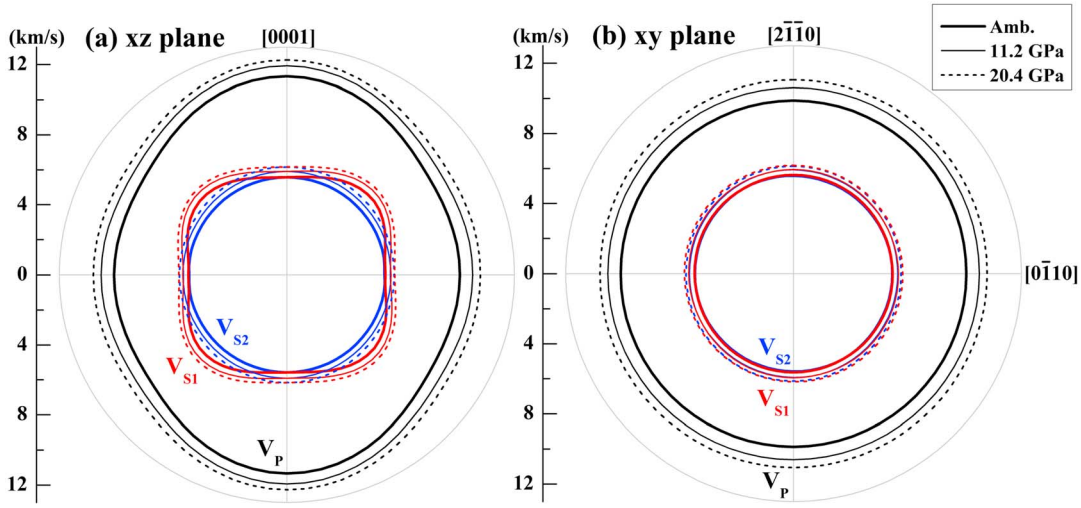

Figure 4. Velocities of the *P* and *S* wave propagation parallel and normal to *c* axis ((a) *x*-*z* and (b) *x*-*y* planes, respectively) for the NAL phase at ambient conditions, 11.2 GPa and 20.4 GPa. The black, red, and blue lines represent the V_P, V_{S1}, and V_{S2}, respectively.

given pressure point [*Mainprice*, 1990; *Mainprice et al*., 2000]. The percentage of V_P, V_{S1}, and V_{S2} anisotropies are defined as

$$\mathrm{AV}_i = \left(V_{i,\ \mathrm{max}} - V_{i,\ \mathrm{min}}\right) / \left(V_{i,\ \mathrm{max}} + V_{i,\ \mathrm{min}}\right) \times 200\ \%, \tag{4}$$

where $i = P$, S_1, or S_2 and $V_{i,\ \mathrm{max}}$ and $V_{i,\ \mathrm{min}}$ represent the maximum and minimum wave velocities in two different propagation directions, respectively. For an anisotropic medium, there are two orthogonally polarized *S* waves with generally different velocities for each propagation direction. Hence, the polarization anisotropy factor of *S* wave (AV_S), also called the shear wave splitting factor, is the anisotropy percentage of the two shear waves' velocities in a given direction and defined as

$$\mathrm{AV}_S = \left(V_{S1} - V_{S2}\right) / \left(V_{S1} + V_{S2}\right) \times 200\ \%, \tag{5}$$

where V_{S1} and V_{S2} are the two orthogonally polarized shear wave velocities in the given propagation direction. Contour upper hemisphere stereograms of V_P, V_{S1}, V_{S2}, AV_S, dV_S ($V_{S1} - V_{S2}$), and V_{S1} polarization for the Fe-bearing NAL phase at ambient conditions and 20.4 GPa are shown in Figure 5. We note that the fastest *P* wave ($V_{P,\ \mathrm{max}} = 11.34$ km/s) propagates along with *c* axis direction and the slowest *P* waves ($V_{P,\ \mathrm{min}} = 9.79$ km/s) distribute in the basal (0001) plane at ambient conditions. The NAL phase is highly anisotropic at ambient conditions, with an AV_P of 14.7% and an AV_S of 15.12% for the Fe-bearing sample and an AV_P of 15.7% and an AV_S of 14.44% for the Fe-free sample. The high AV_S is mainly from the high anisotropy of V_{S1} ($\mathrm{AV}_{S1} = 15.8$~13.9%), while the V_{S2} exhibits very low anisotropies of 0.1~2.8% (Figures 5 and 6 and Table S3). In particular, the V_{S1} ranges from 5.57 to 6.52 km/s, while the V_{S2} ranges from 5.57 to 5.63 km/s at ambient conditions, with a maximum dV_S of 0.92 km/s. At high pressure, the Fe-bearing NAL phase has a similar AV_P but a much larger AV_S than those of Fe-free NAL phase. Although the anisotropy factors of the Fe-free and Fe-bearing NAL phases decrease gradually with increasing pressure, the AV_P and AV_S have high values even at the present maximum pressure, especially the shear wave splitting. For the Fe-free NAL phase, the AV_P is 12.4% and the AV_S is 13.15% at 16.1 GPa, and the Fe-bearing NAL phase has the AV_P of 11.4% and the AV_S of 14.12% at 20.4 GPa (Figure 6 and Table S3).

Using the calculated K_S and G of the NAL phase combined with densities from our previous single-crystal XRD measurements [*Wu et al*., 2016], the aggregate V_P and V_S at high pressure were calculated according to the following equations (Figure 7 and Table S1):

$$VP = \sqrt{\frac{KS + \frac{4}{3}G}{\rho}}; \tag{6}$$

$$VS = \sqrt{\frac{G}{\rho}}, \tag{7}$$

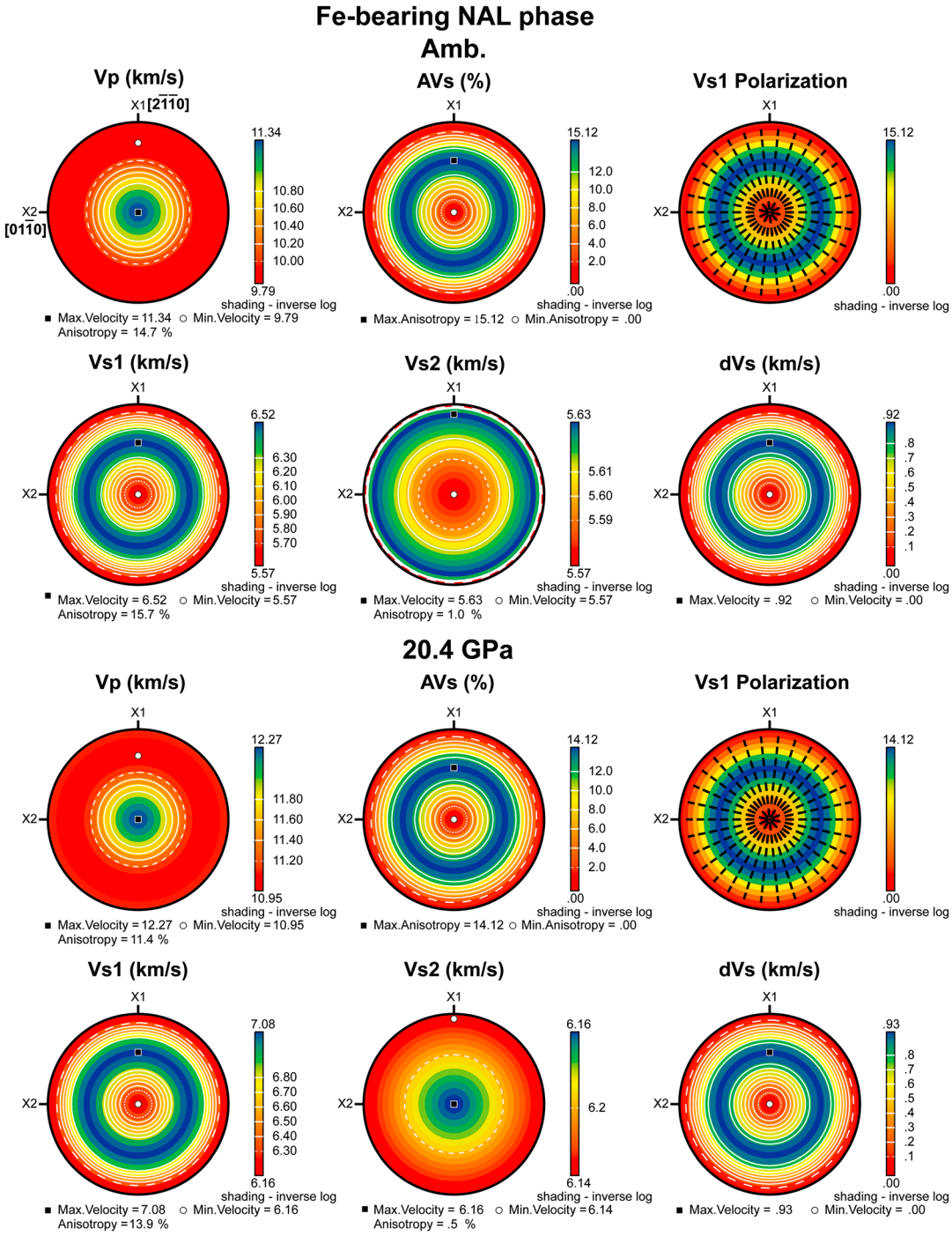

Figure 5. *P* and polarized *S* wave velocities (V_P, V_{S1}, and V_{S2}) distributions, shear wave splitting factors (AV_S), velocity difference of two polarized *S* wave (dV_S), and V_{S1} polarization for the Fe-bearing NAL phase at ambient conditions and 20.4 GPa. All pole figures are the upper hemisphere projections with $X_1 = [2\bar{1}\bar{1}0]$ direction and $X_2 = [01\bar{1}0]$.

where ρ is the density. The NAL phase has aggregate velocities at ambient conditions: $V_P = 10.15(1)$ km/s and $V_S = 5.986(3)$ km/s for the Fe-free NAL phase and $V_P = 10.02(1)$ km/s and $V_S = 5.839(3)$ km/s for the Fe-bearing NAL phase. Aggregate velocities of the Fe-free and Fe-bearing NAL phase increase gradually with increasing pressure. Both V_P and V_S of the Fe-bearing NAL phase are lower than those of the Fe-free NAL phase by ~0.15 km/s.

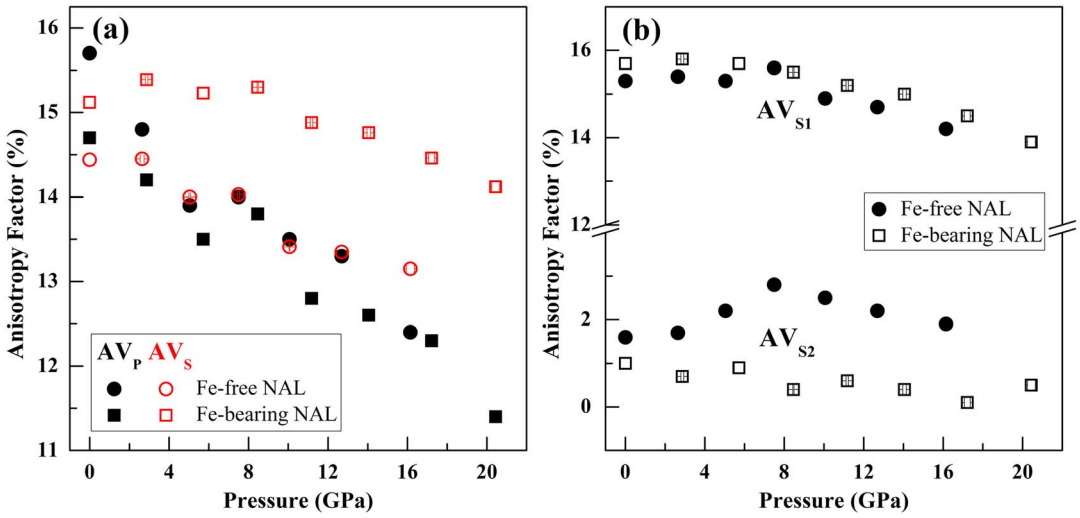

Figure 6. (a) Variation of *P* wave anisotropies and shear wave splitting factors (AV_P and AV_S) and (b) anisotropy factors of two polarized *S* waves (AV_{S1} and AV_{S2}) for the Fe-free and Fe-bearing NAL phases at high pressures.

3.3. Comparison with Previous Studies

The single-crystal and aggregate elastic properties of the NAL phase in this study have been compared to previous results from BLS experiments and theoretical calculations (Table S4) [*Dai et al.*, 2013; *Kawai and Tsuchiya*, 2012; *Mookherjee et al.*, 2012; *Pamato et al.*, 2014]. The elastic moduli (C_{ij}, K_S, and G) and aggregate velocities (V_P and V_S) of the NAL phase in this study are in good agreement with the results from the theoretical calculations of *Kawai and Tsuchiya* [2012] and the BLS experiments of *Pamato et al.* [2014] at ambient conditions (Figures 2, 3, and 7). However, C_{ij}, K_S, and G from the theoretical calculations reported by *Pamato et al.* [2014] are lower than their experimental values (Table S4). *Mookherjee et al.* [2012] reported the elastic properties of the NAL phase with chemical compositions of $KNa_2Al_3Si_3O_{12}$, $NaNa_2Al_3Si_3O_{12}$, and $CaMg_2Al_6O_{12}$ by means of first-principle calculations. C_{11} and C_{12} of $KNa_2Al_3Si_3O_{12}$ and $NaNa_2Al_3Si_3O_{12}$ are substantially lower, while C_{11} of $CaMg_2Al_6O_{12}$ is larger than those of experimental results of this study and *Pamato et al.* [2014] and theoretical results from *Kawai and Tsuchiya* [2012]. This indicates that chemical composition of the NAL phase has a significant effect on its elastic properties (Table S4). Additionally, we note that the seismic velocities reported by *Dai et al.* [2013] from BLS measurements on polycrystalline NAL phase are lower than the BLS experimental results of this study and *Pamato et al.* [2014] (Figure 7). Their reported aggregate V_S of 5.601(5) km/s at ambient conditions is close to the obtained slower *S* wave V_{S2} in this study and *Pamato et al.* [2014]. It is proposed that the BLS measurements of *Dai et al.* [2013] on polycrystalline samples with large intrinsic

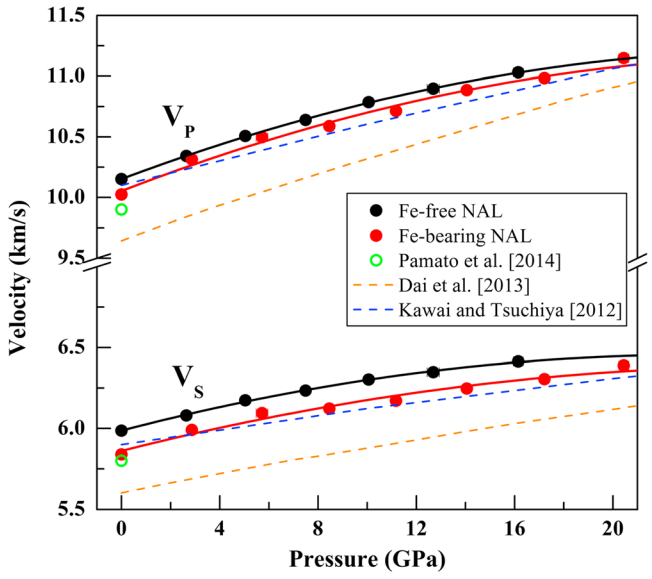

Figure 7. Aggregate velocities (V_P and V_S) of the NAL phase at high pressures and room temperature. Black circles and lines: experimental data and modeled results of the Fe-free NAL phase, respectively (this study); red circles and lines: Fe-bearing NAL (this study); green open circles: *Pamato et al.* [2014]; orange dashed lines: *Dai et al.* [2013]; blue dashed lines: *Kawai and Tsuchiya* [2012].

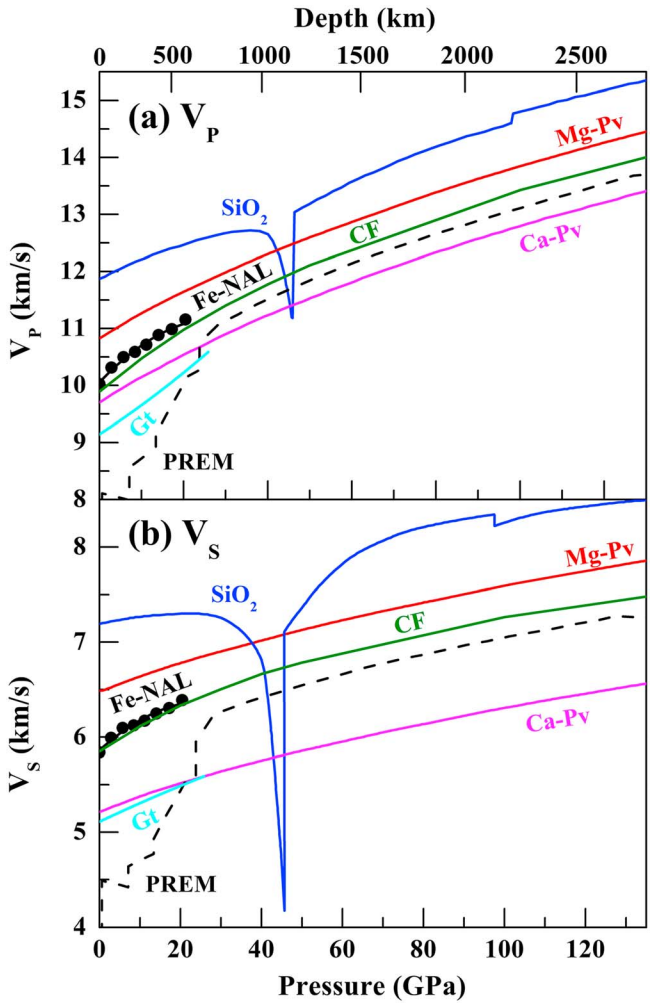

Figure 8. (a) V_P and (b) V_S of the NAL phase at high pressure. Velocities of other major candidate minerals in the lower mantle and PREM are also plotted for comparison. Black: NAL phase; olivine: CF phase [*Dai et al.*, 2013]; red: Mg-Pv [*Murakami et al.*, 2007]; magenta: Ca-Pv [*Kudo et al.*, 2012]; blue: SiO_2 [*Karki et al.*, 1997]; cyan: garnet (Gt) [*Sinogeikin and Bass*, 2000]; dashed lines: PREM [*Dziewonski and Anderson*, 1981].

anisotropy only observed the sharp and slower V_{S2}, where the weak and faster V_{S1} was hidden in the background. Besides V_S, this also reasonably explains the low value of V_P in the study of *Dai et al.* [2013].

4. Implications

4.1. Velocity Profile of the NAL Phase in the Lower Mantle

Seismological studies have indicated the presence of seismic heterogeneities, such as seismic discontinuities and reflectors, or scatterers, in the shallow lower mantle (depths <1200 km) [*Kaneshima*, 2013; *Niu*, 2014; *Vinnik et al.*, 2001]. It is generally proposed that these observations are related to the subducted basalt, in which the NAL phase has been considered as a major mineral [*Ricolleau et al.*, 2010]. To better understand the influence of the presence of the NAL phase on the observed seismic signatures, we have calculated its velocity profiles and compared it to the velocity profiles of other relevant lower mantle minerals and preliminary reference Earth model (PREM; Figure 8) [*Dziewonski and Anderson*, 1981]. The velocity profiles of silica phases do not take into account the influence of Al_2O_3 on the velocities of stishovite- and $CaCl_2$-type phase, since a discrepancy exists among previous studies on the solubility of Al_2O_3 in these SiO_2 polymorphs in the MORB composition [*Ono et al.*, 2001; *Ricolleau et al.*, 2010]. Both V_P and V_S of the NAL phase are lower than those of bridgmanite (Mg-Pv) and SiO_2 [*Karki et al.*, 1997; *Murakami et al.*, 2007] but higher than those of garnet (Gt) and Ca-Pv [*Kudo et al.*, 2012; *Sinogeikin and Bass*, 2000]. The transition in silica from stishovite to the $CaCl_2$-type phase has been used to explain the seismic heterogeneities related to subducted slabs at a depth of ~1200 km without considering the temperature effect [*Niu*, 2014; *Tsuchiya*, 2011] or at 1600~1800 km depths after considering the temperature effect [*Kaneshima and Helffrich*, 1998; *Yang and Wu*, 2014].

Lateral heterogeneities of seismic wave velocities and density have been detected in the deep mantle. These heterogeneities include the shear to compressional wave velocity heterogeneity ratio $R_{S/P} = d\ln V_S/d\ln V_P$, the bulk sound to shear wave velocity heterogeneity ratio $R_{\Phi/S} = d\ln V_\Phi/d\ln V_S$, and the density to velocity heterogeneity ratio $R_{\rho/S} = d\ln\rho/d\ln V_S$ [*Karato and Karki*, 2001]. These heterogeneity ratios can be evaluated to decipher their potential effects of thermal (including anharmonic and anelastic effects) and chemical origins and help understand the role of geodynamic processes on the mantle's seismic profiles. Although thermal effects on the velocity and density profiles of the NAL phase remain lacking, chemical effects due to variation of Fe content can be calculated using our elasticity results. As shown in Figure 9, at room temperature, the $R_{S/P}$ is ~1.9 at 24 GPa, which is much higher than $R_{\Phi/S}$ (~0.1) and $R_{\rho/S}$ (~ −0.1). The $R_{S/P}$ decreases from ~1.9 at 24 GPa

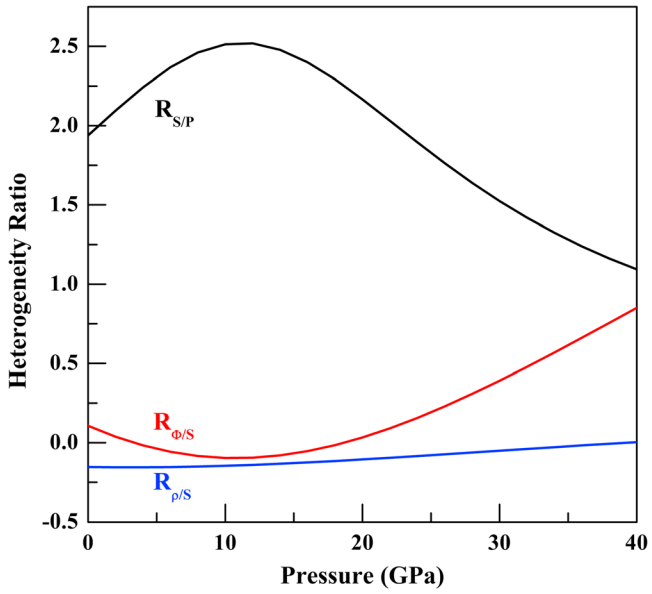

Figure 9. Variation of heterogeneity ratios ($R_{S/P}$, $R_{\Phi/S}$, and $R_{\rho/S}$) at high pressures due to the iron substitution in the NAL phase.

to ~1.1 at 40 GPa; however, the $R_{\Phi/S}$ increases from ~0.1 at 24 GPa to ~0.8 at 40 GPa, and the variation in $R_{\rho/S}$ is small at 24~40 GPa. These results indicate that iron has an increasing and significant effects on $R_{\Phi/S}$. We should note that these modeled ratios do not take into account of the potential effects of the Fe^{3+} spin transition in the NAL phase at 33~47 GPa [*Wu et al.*, 2016].

4.2. Implication for Seismic Anisotropy in the Lower Mantle

There is an increasing evidence for seismic anisotropy inferred from shear wave splitting measurements in the transition zone and the uppermost lower mantle regions around subduction zones [*Foley and Long*, 2011; *Wookey and Kendall*, 2004; *Wookey et al.*, 2002], although these regions were previously believed to be seismically isotropic [*Fischer and Wiens*, 1996]. The observed anisotropy in the midmantle is usually interpreted to be related to mantle flow and subducted slabs, in which large stresses associated with mantle convection and the subduction process could exist in the surrounding mantle and subducted slabs. These could induce the lattice-preferred orientation of the constituting minerals or shape-preferred orientation of inclusions. There are a number of potential causes for midmantle anisotropy that have been proposed, including the moderately anisotropic wadsleyite [*Faccenda*, 2014; *Kawazoe et al.*, 2013], dislocation creep of bridgmanite [*Cordier et al.*, 2004; *Wenk et al.*, 2004], and/or highly anisotropic phase D [*Rosa et al.*, 2013].

Experimental studies on single-crystal elastic and seismic properties of the mantle minerals at high pressures play a significant role in understanding the seismic signatures of subducted slabs. To decipher the potential significance of the NAL phase on the observed seismic anisotropy in the uppermost lower mantle, we have calculated the AV_P and AV_S of the NAL phase at 40 GPa corresponding to a depth of ~1000 km using the obtained elastic constants and their pressure derivatives. The AV_P and AV_S of the Fe-free NAL phase at 40 GPa are 9.2% and 9.62%, respectively, and the AV_P and AV_S of the high-spin Fe-bearing NAL phase at 40 GPa are 14.9% and 15.6%, respectively. The anisotropies of Fe-free or high-spin Fe-bearing NAL phase at 40 GPa are larger than those of bridgmanite (8%) at the same pressure [*Mainprice*, 2007; *Wentzcovitch et al.*, 2004], while the AV_S of the NAL phase is smaller than those of Ca-Pv (~22%) at 40 GPa [*Kawai and Tsuchiya*, 2015]. We should caution that the extrapolation of the velocity anisotropies is only for the high-spin Fe-bearing NAL phase, which does not take into account of the potential spin transition effects on the elasticity. In our previous study, the octahedral Fe^{3+} (~1.5 mol%) in the Fe-bearing NAL phase (the same sample as in this study) undergoes a high-spin to low-spin transition at 30~40 GPa, which causes the elastic and velocity softening of the Fe-bearing NAL phase. The bulk sound velocity softening (maximum 9.4%) of the Fe-bearing NAL phase can contribute to the velocity softening of the MORB composition by up to 2% [*Wu et al.*, 2016].

The NAL and CF phases coexist at pressures ranging from ~30 to ~50 GPa (~1200 km), above which only the CF phase is observed to be stable. Based on the mineral proportion of the subducted MORB in the lower mantle [*Ricolleau et al.*, 2010], the NAL and CF phases constitute 10–30 wt% of the MORB composition; the amount of the NAL phase decreases from about 20 wt% at ~25 GPa to 15 wt% at ~40 GPa. The considerably high amount of the aluminous phases in the MORB and their distinct high-pressure behavior (including octahedral Fe^{3+} spin transitions and potential NAL-to-CF phase transition) can have significant effects on the velocity profiles and seismic anisotropies of the MORB composition in the lower mantle. Thus, based on our previous

and present studies, we propose that the aluminous phases in the MORB can play a significant role in the lower mantle and that the NAL phase can contribute to the observed seismic anisotropy in subducted slabs at the top regions of the lower mantle.

5. Conclusions

In summary, the full set of elastic constants of the single-crystal NAL phase with $Na_{1.14}Mg_{1.83}Al_{4.74}Si_{1.23}O_{12}$ and $Na_{0.71}Mg_{2.05}Al_{4.62}Si_{1.16}Fe^{2+}_{0.09}Fe^{3+}_{0.17}O_{12}$ compositions has been determined using BLS coupled with DACs at pressures up to 20 GPa and room temperature. These results provide experimental constraints on the pressure and iron substitution effects on the elastic moduli, velocity profiles, and anisotropies of the NAL phase at high pressure. All of the five independent elastic constants increase with increasing pressure at room temperature. The elastic and seismic properties of single-crystal NAL phase at high pressure were modeled and applied to decipher the observed seismic anisotropy around subducted slabs in the lower mantle at depths below 1200 km. We found that the NAL phase with its high seismic anisotropy, especially its high shear wave splitting, may be a potential source of the observed seismic anisotropy around subducted slabs in the uppermost lower mantle. The present results of this study provide a new insight into the seismic structure of the Earth's lower mantle.

Acknowledgments

We thank C. McCammon for helping with the Mössbauer analysis of the Fe-bearing NAL phase sample. H. Huang acknowledges financial support from 973 Program of China (2014CB845904). X. Wu acknowledges financial support from the National Science Foundation of China (U1232204 and 41473056). M. Song acknowledges support by the Strategic Priority Research Program (B) of the Chinese Academy of Sciences (XDB18010402). J.-F. Lin acknowledges support from the U.S. National Science Foundation Geophysics Program and HPSTAR. Data used in this study are available from Xiang Wu (e-mail: wuxiang@cug.edu.cn) and Ye Wu (e-mail: yew@whut.edu.cn) upon request.

References

Birch, F. (1978), Finite strain isotherm and velocities for single-crystal and polycrystalline NaCl at high pressures and 300 K, *J. Geophys. Res.*, *83*(B3), 1257–1268, doi:10.1029/JB083iB03p01257.

Cordier, P., T. Ungár, L. Zsoldos, and G. Tichy (2004), Dislocation creep in $MgSiO_3$ perovskite at conditions of the Earth's uppermost lower mantle, *Nature*, *428*(6985), 837–840, doi:10.1038/nature02472.

Dai, L., Y. Kudo, K. Hirose, M. Murakami, Y. Asahara, H. Ozawa, Y. Ohishi, and N. Hirao (2013), Sound velocities of $Na_{0.4}Mg_{0.6}Al_{1.6}Si_{0.4}O_4$ NAL and CF phases to 73 GPa determined by Brillouin scattering method, *Phys. Chem. Miner.*, *40*(3), 195–201, doi:10.1007/s00269-012-0558-0.

Dziewonski, A. M., and D. L. Anderson (1981), Preliminary reference Earth model, *Phys. Earth Planet. Inter.*, *25*(4), 297–356, doi:10.1016/0031-9201(81)90046-7.

Every, A. (1980), General closed-form expressions for acoustic waves in elastically anisotropic solids, *Phys. Rev. B*, *22*(4), 1746, doi:10.1103/PhysRevB.22.1746.

Faccenda, M. (2014), Mid mantle seismic anisotropy around subduction zones, *Phys. Earth Planet. Inter.*, *227*, 1–19, doi:10.1016/j.pepi.2013.11.015.

Fischer, K. M., and D. A. Wiens (1996), The depth distribution of mantle anisotropy beneath the Tonga subduction zone, *Earth Planet. Sci. Lett.*, *142*(1), 253–260, doi:10.1016/0012-821X(96)00084-2.

Foley, B. J., and M. D. Long (2011), Upper and mid-mantle anisotropy beneath the Tonga slab, *Geophys. Res. Lett.*, *38*, L02303, doi:10.1029/2010GL046021.

Fukao, Y., and M. Obayashi (2013), Subducted slabs stagnant above, penetrating through, and trapped below the 660 km discontinuity, *J. Geophys. Res. Solid Earth*, *118*, 5920–5938, doi:10.1002/2013JB010466.

Green, D., W. Hibberson, and A. Jaques (1979), Petrogenesis of mid-ocean ridge basalts, in *The Earth: Its Origin, Structure and Evolution*, edited by D. H. Green, W. O. Hibberson, and A. L. Jaques, pp. 265–299, Academic Press, London.

Guignot, N., and D. Andrault (2004), Equations of state of Na–K–Al host phases and implications for MORB density in the lower mantle, *Phys. Earth Planet. Inter.*, *143-144*, 107–128, doi:10.1016/j.pepi.2003.09.014.

Hill, R. (1952), The elastic behaviour of a crystalline aggregate, *Proc. Phys. Soc. Sect. A*, *65*(5), 349, doi:10.1088/0370-1298/65/5/307.

Hirose, K., and Y. Fei (2002), Subsolidus and melting phase relations of basaltic composition in the uppermost lower mantle, *Geochim. Cosmochim. Acta*, *66*(12), 2099–2108, doi:10.1016/S0016-7037(02)00847-5.

Hirose, K., N. Takafuji, N. Sata, and Y. Ohishi (2005), Phase transition and density of subducted MORB crust in the lower mantle, *Earth Planet. Sci. Lett.*, *237*(1), 239–251, doi:10.1016/j.epsl.2005.06.035.

Imada, S., K. Hirose, and Y. Ohishi (2011), Stabilities of NAL and Ca-ferrite-type phases on the join $NaAlSiO_4$-$MgAl_2O_4$ at high pressure, *Phys. Chem. Miner.*, *38*(7), 557–560, doi:10.1007/s00269-011-0427-2.

Irifune, T., and A. Ringwood (1993), Phase transformations in subducted oceanic crust and buoyancy relationships at depths of 600–800 km in the mantle, *Earth Planet. Sci. Lett.*, *117*(1), 101–110, doi:10.1016/0012-821X(93)90120-X.

Kaneshima, S. (2013), Lower mantle seismic scatterers below the subducting Tonga slab: Evidence for slab entrainment of transition zone materials, *Phys. Earth Planet. Inter.*, *222*, 35–46, doi:10.1016/j.pepi.2013.07.001.

Kaneshima, S., and G. Helffrich (1998), Detection of lower mantle scatterers northeast of the Marianna subduction zone using short-period array data, *J. Geophys. Res.*, *103*(B3), 4825–4838, doi:10.1029/97JB02565.

Karato, S. I., and B. B. Karki (2001), Origin of lateral variation of seismic wave velocities and density in the deep mantle, *J. Geophys. Res.*, *106*(R10), 21,771–21,783, doi:10.1029/2001JB000214.

Karki, B. B., L. Stixrude, and J. Crain (1997), Ab initio elasticity of three high-pressure polymorphs of silica, *Geophys. Res. Lett.*, *24*(24), 3269–3272, doi:10.1029/97GL53196.

Kawai, K., and T. Tsuchiya (2012), Phase stability and elastic properties of the NAL and CF phases in the $NaMg_2Al_5SiO_{12}$ system from first principles, *Am. Mineral.*, *97*(2-3), 305–314, doi:10.2138/am.2012.3915.

Kawai, K., and T. Tsuchiya (2015), Small shear modulus of cubic $CaSiO_3$ perovskite, *Geophys. Res. Lett.*, *42*, 2718–2726, doi:10.1002/2015GL063446.

Kawakatsu, H., and F. Niu (1994), Seismic evidence for a 920-km discontinuity in the mantle, *Nature*, *371*(6495), 301–305, doi:10.1038/371301a0.

Kawazoe, T., T. Ohuchi, Y. Nishihara, N. Nishiyama, K. Fujino, and T. Irifune (2013), Seismic anisotropy in the mantle transition zone induced by shear deformation of wadsleyite, *Phys. Earth Planet. Inter.*, *216*, 91–98, doi:10.1016/j.pepi.2012.12.005.

Kudo, Y., K. Hirose, M. Murakami, Y. Asahara, H. Ozawa, Y. Ohishi, and N. Hirao (2012), Sound velocity measurements of $CaSiO_3$ perovskite to 133 GPa and implications for lowermost mantle seismic anomalies, *Earth Planet. Sci. Lett.*, *349*, 1–7, doi:10.1016/j.epsl.2012.06.040.

Lu, C., Z. Mao, J.-F. Lin, K. K. Zhuravlev, S. N. Tkachev, and V. B. Prakapenka (2013), Elasticity of single-crystal iron-bearing pyrope up to 20 GPa and 750 K, *Earth Planet. Sci. Lett.*, *361*, 134–142, doi:10.1016/j.epsl.2012.11.041.

Mainprice, D. (1990), A FORTRAN program to calculate seismic anisotropy from the lattice preferred orientation of minerals, *Comput. Geosci.*, *16*(3), 385–393, doi:10.1016/0098-3004(90)90072-2.

Mainprice, D. (2007), Seismic anisotropy of the deep Earth from a mineral and rock physics perspective, in *Treatise in Geophysics-Volume 2 Mineral Physics*, edited by G. Schubert, pp. 437–492, Elsevier, Oxford.

Mainprice, D., G. Barruol, and W. B. Ismaïl (2000), The seismic anisotropy of the Earth's mantle: From single crystal to polycrystal, in *Earth's Deep Interior: Mineral Physics and Tomography From the Atomic to the Global Scale*, vol. 117, edited by S.-I. Karato et al., pp. 237-264, AGU, Washington, D. C., doi:10.1029/GM117p0237.

Mao, H. K., J. Xu, and P. M. Bell (1986), Calibration of the ruby pressure gauge to 800-kbar under quasi-hydrostatic conditions, *J. Geophys. Res.*, *91*(B5), 4673–4676, doi:10.1029/JB091iB05p04673.

Miura, H., Y. Hamada, T. Suzuki, M. Akaogi, N. Miyajima, and K. Fujino (2000), Crystal structure of $CaMg_2Al_6O_{12}$, a new Al-rich high pressure form, *Am. Mineral.*, *85*, 1799–1803, doi:10.2138/am-2000-11-1223.

Miyajima, N., K. Fujino, N. Funamori, T. Kondo, and T. Yagi (1999), Garnet-perovskite transformation under conditions of the Earth's lower mantle: An analytical transmission electron microscopy study, *Phys. Earth Planet. Inter.*, *116*, 117–131, doi:10.1016/S0031-9201(99)00127-2.

Mookherjee, M., B. B. Karki, L. Stixrude, and C. Lithgow-Bertelloni (2012), Energetics, equation of state, and elasticity of NAL phase: Potential host for alkali and aluminum in the lower mantle, *Geophys. Res. Lett.*, *39*, L19306, doi:10.1029/2012GL053682.

Murakami, M., S. V. Sinogeikin, H. Hellwig, J. D. Bass, and J. Li (2007), Sound velocity of $MgSiO_3$ perovskite to Mbar pressure, *Earth Planet. Sci. Lett.*, *256*(1), 47–54, doi:10.1016/j.epsl.2007.01.011.

Musgrave, M. J. (1970), *Crystal Acoustics*, 289pp., Holden-Day, San Francisco.

Niu, F. (2014), Distinct compositional thin layers at mid-mantle depths beneath northeast China revealed by the USArray, *Earth Planet. Sci. Lett.*, *402*, 305–312, doi:10.1016/j.epsl.2013.02.015.

Ono, A., M. Akaogi, H. Kojitani, K. Yamashita, and M. Kobayashi (2009), High-pressure phase relations and thermodynamic properties of hexagonal aluminous phase and calcium-ferrite phase in the systems $NaAlSiO_4$–$MgAl_2O_4$ and $CaAl_2O_4$–$MgAl_2O_4$, *Phys. Earth Planet. Inter.*, *174*(1), 39–49, doi:10.1016/j.pepi.2008.07.028.

Ono, S., E. Ito, and T. Katsura (2001), Mineralogy of subducted basaltic crust (MORB) from 25 to 37 GPa, and chemical heterogeneity of the lower mantle, *Earth Planet. Sci. Lett.*, *190*(1), 57–63, doi:10.1016/S0012-821X(01)00375-2.

Ono, S., Y. Ohishi, M. Isshiki, and T. Watanuki (2005), In situ X-ray observations of phase assemblages in peridotite and basalt compositions at lower mantle conditions: Implications for density of subducted oceanic plate, *J. Geophys. Res.*, *110*, B02208, doi:10.1029/2004JB003196.

Pamato, M. G., A. Kurnosov, T. B. Ballaran, D. M. Trots, R. Caracas, and D. J. Frost (2014), Hexagonal $Na_{0.41}[Na_{0.125}Mg_{0.79}Al_{0.085}]_2[Al_{0.79}Si_{0.21}]_6O_{12}$ (NAL phase): Crystal structure refinement and elasticity, *Am. Mineral.*, *99*(8-9), 1562–1569, doi:10.2138/am.2014.4755.

Poirier, J. P. (2000), *Introduction to the Physics of the Earth's Interior*, Cambridge Univ. Press, Cambridge.

Ricolleau, A., J. P. Perrillat, G. Fiquet, I. Daniel, J. Matas, A. Addad, N. Menguy, H. Cardon, M. Mezouar, and N. Guignot (2010), Phase relations and equation of state of a natural MORB: Implications for the density profile of subducted oceanic crust in the Earth's lower mantle, *J. Geophys. Res.*, *115*, B08202, doi:10.1029/2009JB006709.

Rosa, A. D., C. Sanchez-Valle, C. Nisr, S. R. Evans, R. Debord, and S. Merkel (2013), Shear wave anisotropy in textured phase D and constraints on deep water recycling in subduction zones, *Earth Planet. Sci. Lett.*, *377-378*, 13–22, doi:10.1016/j.epsl.2013.06.036.

Shannon, R. D. (1976), Revised effective ionic radii and systematic studies of interatomic distances in halides and chalcogenides, *Acta Crystallogr., Sect. A*, *32*(5), 751–767, doi:10.1107/s0567739476001551.

Shinmei, T., T. Sanehira, D. Yamazaki, T. Inoue, T. Irifune, K. Funakoshi, and A. Nozawa (2005), High-temperature and high-pressure equation of state for the hexagonal phase in the system $NaAlSiO_4$–$MgAl_2O_4$, *Phys. Chem. Miner.*, *32*(8-9), 594–602, doi:10.1007/s00269-005-0029-y.

Sinogeikin, S. V., and J. D. Bass (2000), Single-crystal elasticity of pyrope and MgO to 20 GPa by Brillouin scattering in the diamond cell, *Phys. Earth Planet. Inter.*, *120*(1–2), 43–62, doi:10.1016/S0031-9201(00)00143-6.

Sun, S. S. (1982), Chemical composition and origin of the Earth's primitive mantle, *Geochim. Cosmochim. Acta*, *46*(2), 179–192, doi:10.1016/0016-7037(82)90245-9.

Tsuchiya, T. (2011), Elasticity of subducted basaltic crust at the lower mantle pressures: Insights on the nature of deep mantle heterogeneity, *Phys. Earth Planet. Inter.*, *188*(3), 142–149, doi:10.1016/j.pepi.2011.06.018.

Vinnik, L., M. Kato, and H. Kawakatsu (2001), Search for seismic discontinuities in the lower mantle, *Geophys. J. Int.*, *147*(1), 41–56, doi:10.1046/j.1365-246X.2001.00516.x.

Walter, M. J., S. C. Kohn, D. Araujo, G. P. Bulanova, C. B. Smith, E. Gaillou, J. Wang, A. Steele, and S. B. Shirey (2011), Deep mantle cycling of oceanic crust: Evidence from diamonds and their mineral inclusions, *Science*, *334*(6052), 54–57, doi:10.1126/science.1209300.

Wenk, H. R., I. Lonardeli, J. Pehl, J. Devine, V. Prakapenka, G. Shen, and H. K. Mao (2004), In situ observation of texture development in olivine, ringwoodite, magnesiowüstite and silicate perovskite at high pressure, *Earth Planet. Sci. Lett.*, *226*(3–4), 507–519, doi:10.1016/j.epsl.2004.07.033.

Wentzcovitch, R., B. Karki, M. Cococcioni, and S. De Gironcoli (2004), Thermoelastic properties of $MgSiO_3$ perovskite: Insights on the nature of the Earth's lower mantle, *Phys. Rev. Lett.*, *92*(1), 018,501, doi:10.1103/PhysRevLett.92.018501.

Wookey, J., and J. M. Kendall (2004), Evidence of midmantle anisotropy from shear wave splitting and the influence of shear-coupled *P* waves, *J. Geophys. Res.*, *109*, B07309, doi:10.1029/2003JB002871.

Wookey, J., J. M. Kendall, and G. Barruol (2002), Mid-mantle deformation inferred from seismic anisotropy, *Nature*, *415*(6873), 777–780, doi:10.1038/415777a.

Wu, Y., X. Wu, J.-F. Lin, C. A. McCammon, Y. Xiao, P. Chow, V. B. Prakapenka, T. Yoshino, S. Zhai, and S. Qin (2016), Spin transition of ferric iron in the NAL phase: Implications for the seismic heterogeneities of subducted slabs in the lower mantle, *Earth Planet. Sci. Lett.*, *434*, 91–100, doi:10.1016/j.epsl.2015.11.011.

Yang, J., X. Tong, J.-F. Lin, T. Okuchi, and N. Tomioka (2015), Elasticity of ferropericlase across the spin crossover in the Earth's lower mantle, *Sci. Rep.*, *5*, 17,188, doi:10.1038/srep17188.

Yang, R., and Z. Wu (2014), Elastic properties of stishovite and the $CaCl_2$-type silica at the mantle temperature and pressure: An ab initio investigation, *Earth Planet. Sci. Lett.*, *404*, 14–21, doi:10.1016/j.epsl.2014.07.020.

Zhao, D. P. (2004), Global tomographic images of mantle plumes and subducting slabs: Insight into deep Earth dynamics, *Phys. Earth Planet. Inter.*, *146*(1-2), 3–34, doi:10.1016/j.pepi.2003.07.032.